

**Vertical Structure of Tropical Cyclones with Concentric Eyewalls as seen by the TRMM  
Precipitation Radar**

Deanna A. Hence and Robert A. Houze, Jr.  
University of Washington, Seattle, Washington

Submitted to Journal of Atmospheric Sciences  
April 2011  
Revised August 2011

*Corresponding author address:* Deanna Hence, Department of Atmospheric Sciences, University  
of Washington, Box 351640, Seattle, WA 98195  
E-mail: [dhence@atmos.washington.edu](mailto:dhence@atmos.washington.edu)

## **Abstract**

Ten years of data from the Tropical Rainfall Measurement Mission satellite's Precipitation Radar are analyzed to determine the typical vertical structure of the concentric eyewalls of tropical cyclones undergoing eyewall replacement. The vertical structure of the secondary (outer) eyewall is different from the primary (inner) eyewall and also different from the eyewall of single eyewall storms. The upper-troposphere portions of the outer eyewalls are like the rainbands from which they evolve. Their lower-tropospheric portions are more intense and more uniform than rainbands of single eyewall storms, suggesting that these secondary eyewalls are forming from rainbands undergoing axisymmetrization and building from below. The inner concentric eyewalls are more strongly affected by shear than are the eyewalls of single eyewall storms, while the outer eyewalls are relatively unaffected by shear, which suggests the outer eyewall is amplifying the shear-induced asymmetry of the inner eyewall.

1 **1. Introduction**

2 Typically the inner regions of a mature tropical cyclone exhibit one clearly defined eyewall  
3 and one or two large principal rainbands, with the occasional presence of smaller intense  
4 secondary bands (Willoughby 1988; Houze 2010). A bridge of light stratiform precipitation can  
5 provide a connection between the eyewall's intense ring of convective precipitation and the  
6 mixture of heavier stratiform precipitation and pockets of convection in the rainband complex  
7 (Marks and Houze 1987), although in more intense storms this region between the eyewall and  
8 the rainbands is sometimes precipitation-free (Willoughby et al. 1984). This common  
9 configuration of storms exhibiting a single eyewall changes with the development of concentric  
10 eyewalls. In concentric eyewall cases, a quasi-circular region of high reflectivity and a  
11 corresponding wind maximum form outside of, and concentric to, the primary (inner) eyewall  
12 region (Willoughby et al. 1982). A light precipitation or precipitation-free lane, commonly  
13 known as the moat, forms between this secondary eyewall and the primary eyewall. If a full  
14 eyewall-replacement cycle occurs, this secondary eyewall contracts and induces subsidence in  
15 the region immediately outside the primary eyewall. The secondary (outer) eyewall eventually  
16 takes over when the primary eyewall dissipates (Shapiro and Willoughby 1982; Willoughby et  
17 al. 1982; Houze et al. 2007b), although occasionally this eyewall replacement fails (Willoughby  
18 1990).

19 Since the eyewall replacement cycle seems to occur most frequently in intense storms and  
20 has significant impacts upon the vorticity, wind, and heating distribution within the storm,  
21 understanding this process is critical for improving intensity prediction and understanding  
22 tropical cyclone dynamics. Several observational case studies have documented the eyewall

1 replacement process once it is underway (Black et al. 1972; Black and Willoughby 1992;  
2 Franklin et al. 1993; Dodge et al. 1999), although only recently has high resolution direct dual-  
3 Doppler analysis of a concentric eyewall case become available (Houze et al. 2007b; Didlake  
4 and Houze 2011). Several modeling studies provided significant insights into the possible  
5 dynamics governing eyewall replacement (Kossin et al. 2000; Rozoff et al. 2006; Rozoff et al.  
6 2008; Terwey and Montgomery 2008; Judt and Chen 2010; Qiu et al. 2010). Until recently  
7 (Houze et al. 2007b), the short duration of the process (typically about 12 h) and the lack of  
8 predictability in real-time make in situ observations of concentric eyewall behavior and  
9 confirmation of those modeling results difficult. Some attempts have therefore been made in  
10 using satellite techniques to study concentric eyewalls (Kuo et al. 2009), but they rely on passive  
11 microwave data that lack the three-dimensional structure of the convective features being  
12 studied.

13 This study statistically analyzes 1997-2007 data collected by the Tropical Rainfall  
14 Measurement Mission satellite's Precipitation Radar (the TRMM PR; see Kummerow et al. 1998  
15 for details) in the Atlantic and northwest (NW) Pacific basins. The objective of the research is to  
16 take advantage of the long-term statistics offered by the TRMM PR to compensate for the lack of  
17 time continuity in the data on any one storm. The vertical distribution of precipitation revealed  
18 by the active high-resolution PR dataset provides insight into the common precipitation features  
19 seen within concentric eyewalls and vertical structure information unavailable in other satellite  
20 data, thus providing a baseline comparison for observational and modeling studies. After  
21 describing our dataset and methods of analysis in Section 2, Section 3 details the general features  
22 of the primary eyewall, moat, and secondary eyewall. Section 4 compares the asymmetric  
23 structure of a single eyewall with the asymmetric structure of the primary eyewall and the

1 secondary eyewall in concentric eyewall cases. In Section 5 we synthesize the results and present  
2 our conclusions.

### 3 **2. The TRMM PR, CFADs, radial and quadrant analysis**

4 We use the TRMM PR Version 6 2A25 reflectivity data (TSDIS 2007) to obtain a three-  
5 dimensional view of reflectivity structure. The ~250 m resolution (at nadir) of the PR makes it  
6 ideal for evaluating changes in the vertical distribution of precipitation. The ~215/247 km swath  
7 width (before/after the boost in orbital altitude that occurred in August 2001) and the roughly  
8 twice daily sampling (for a given location) have provided numerous overpasses of tropical  
9 cyclones. The horizontal resolution is 4.3/5 km (pre-/post-boost). Since the focus of this study is  
10 on the vertical structure of precipitation, the change in horizontal resolution does not affect the  
11 results significantly; however, the larger swath width advantageously provides a somewhat more  
12 complete view of any single storm.

13 Following Houze et al. (2007a), we remapped the PR reflectivity data onto a Cartesian grid  
14 after applying small corrections to the geolocation of the upper-level data. Cartesian gridding  
15 allows for visualization in the NCAR Zebra software (Corbet et al. 1994; James et al. 2000) and  
16 facilitates computation of Contoured Frequency by Altitude Diagrams (CFADs, Yuter and  
17 Houze 1995). Reflectivity values in the Cartesian grid were counted in 1 dB bins every 0.25 km  
18 in height. We only included reflectivity data above the minimal detection of the radar (~17-18  
19 dBZ).

20 As in Hance and Houze (2011), we use CFADs to display the binned reflectivity values.  
21 CFADs are joint probability distributions that allow for the accumulation of data from numerous  
22 overpasses in a single plot while taking advantage of the PR's high resolution in the vertical. The

1 mean, standard deviation, skewness and excess kurtosis (kurtosis–3; see DeCarlo 1997) are  
2 calculated on these raw CFADs. For plotting purposes, the CFADs were normalized by the  
3 maximum frequency in the sample (Houze et al. 2007a; Hense and Houze 2011). Dividing all the  
4 bins by the maximum frequency in the distribution removes the effect of the bulk amount of  
5 radar echo in a given subset of the data, as well as bringing any peaks in the distribution to the  
6 same magnitude for each computed CFAD. This normalization does not change the shape of the  
7 distribution, but it allows every profile to be plotted on the same scale. A more complete  
8 discussion of this normalization is included in Hense and Houze (2011).

9 This study uses the storm center, intensity, and eye diameter from the International Best  
10 Track Archive for Climate Stewardship (Knapp et al. 2010). Our analysis includes TRMM  
11 overpasses of storms within the Atlantic and NW Pacific basins between 1998-2007 that reached  
12 Category 4 ( $59\text{-}69\text{ m s}^{-1}$ ; Saffir 2003) or 5 ( $> 69\text{ m s}^{-1}$ ) sometime during their lifetimes. Only  
13 overpasses occurring when the storm intensity was at least Category 1 (maximum sustained wind  
14  $> 32\text{ m s}^{-1}$ ) are included. We estimated conditions and storm position at TRMM overpass times  
15 via simple interpolation between observations bracketing the time of overpass. The overpass  
16 samples are referred to by the status of the storm *at the time of the overpass*. All of the  
17 overpasses included in this study have the storm center contained within the TRMM Microwave  
18 Imager's swath width (TMI, Kummerow et al. 1998; 760 km pre-boost, 878 km post-boost). The  
19 TMI 37 and 85 GHz data and the PR data (when available) were used together to identify  
20 concentric eyewall cases and to determine eye diameters when necessary. Since the 37 GHz  
21 channel is sensitive to rain, this gives us an estimate of the eye diameter closer to the surface  
22 than the 85.5 GHz channel, but they are used in combination because of the 37 GHz channel's  
23 low resolution. In the case of an eyewall with broken echo coverage, estimates of the eye

1 diameter are made on the inner edge of the feature exhibiting the geometry of the arc of a circle  
2 or ellipse. For an elliptical eyewall, the long and short axis average is used to define eyewall size.  
3 The storm center from the best-track data is visually checked against the PR and TMI data, since  
4 the circulation center of the storm often does not necessarily match the center of the precipitation  
5 feature (Bluestein and Marks 1987). If necessary, the center of the analysis is manually shifted to  
6 better align with the precipitation features.

7 Data from 65 storms (26 Atlantic, 39 NW Pacific) included 37 overpasses of storms  
8 exhibiting concentric eyewalls. The criteria used to determine concentric eyewall cases were: 1)  
9 a ring of high reflectivity existing outside of the eyewall having low-level reflectivity intensities  
10 similar to those of the primary eyewall; 2) a still-present primary eyewall, although a complete  
11 circle of reflectivity was not required; 3) concentric eyewalls having circular geometry, meaning  
12 that the reflectivity feature did not depart from the boundaries of an annular region defined by  
13 the objective method below, to distinguish them from spiraling rainbands; and 4) the innermost  
14 regions of the storm at least partially covered by the TRMM PR. Because of this last criterion, all  
15 of the 37 overpasses contain data from the primary eyewall, moat, and secondary eyewall. All  
16 cases not meeting these four criteria were considered single eyewall cases.

17 Applying these criteria, a total of 371 overpasses of single eyewall cases were identified.  
18 However, since the TMI and PR swaths are much different in width, only 164 overpasses of the  
19 single eyewall cases contain PR data in the eyewall region. For these cases, the storm-center and  
20 eye-diameter reports establish the eye radius  $R_e$ , which marks the inner boundary for the eyewall  
21 region 1. As in Hance and Houze (2011), we divide the storm into a series of annuli of increasing  
22 diameter. The outer edge of the first annulus ( $R_1$ ) assumes a  $45^\circ$  slope of the eyewall (Marks and  
23 Houze 1987) with flow up to a tropopause height of 17 km (Jordan 1958), defining  $R_1$  as  $R_1 = R_e$

1 + 17 km. This constant eyewall width was selected to provide the best chance of capturing the  
2 full sloping eyewall and the precipitation directly underneath. Eight subsequent annuli are  
3 defined by their outer boundaries, which are multiples of  $R_1$ , such that  $R_2 = 2R_1$ ,  $R_3 = 3R_1 \dots$ ,  $R_9$   
4  $= 9R_1$ . An example of this method is illustrated in the first figure of Hence and Houze (2011).  
5 Because of particle advection away from the storm center, the eye estimates may bias slightly  
6 large, resulting in a slight bias in the region definitions, but the bias would be small relative to  
7 the area each region covers.

8 Statistics are computed for each of the nine annular regions. The objective technique used by  
9 Hence and Houze (2011) to determine the annular regions for single eyewall cases, although  
10 attempted, did not suffice to generate statistics for the concentric eyewall cases because the  
11 width of the moat and the location of the secondary eyewall were variable. To clarify the  
12 statistics, we subjectively adjusted the boundaries of the primary eyewall ( $R_1$ ), the moat ( $R_2$ ), and  
13 the secondary eyewall ( $R_3$ ) on the basis of their PR and TMI presentation. The average  
14 dimensions of the three regions, and their single eyewall counterparts, are listed in Table 1.

15 As in Hence and Houze (2011), this study uses a quadrant-by-quadrant analysis to study how  
16 features vary around the storm. As in our previous study, the quadrants are oriented by the 850-  
17 200 hPa shear vector, calculated from the National Centers for Environmental Prediction  
18 (NCEP) Reanalysis zonal (u) and meridional (v) winds (Kalnay et al. 1996). The 200 hPa wind  
19 vectors were subtracted from the 850 hPa wind vectors at every point within a ring of wind data  
20 500-750 km from the storm center, to avoid the influence of the storm's circulation. These  
21 individual shear vectors were then vector-averaged to create the mean shear vector and  
22 interpolated (using the interpolation method described above) to estimate the shear at the time of  
23 the overpass. The quadrants are defined counter-clockwise from the direction of this mean shear

1 vector. The averages of these interpolated shear vectors for the respective samples are shown in  
2 Table 1. This mean shear calculation was also performed for a ring 200-800 km from the storm  
3 center, as done in Chen et al. (2006), and our results are strongly consistent with theirs.  
4 However, the 500-750 km ring was used to eliminate, as much as possible, the influence of the  
5 storm's wind field.

### 6 **3. Structure of the primary eyewall, moat, and secondary eyewall**

7 To characterize the unique features of concentric eyewall cases, we compare the reflectivity  
8 CFADs of the inner three regions of the concentric eyewall cases with those from the single  
9 eyewall cases. The left column of Fig. 1 shows the normalized total accumulation CFADs of the  
10 concentric eyewall cases' primary eyewall (region 1, Fig. 1a), moat (region 2, Fig. 1c), and  
11 secondary eyewall (region 3, Fig. 1e) regions. The right column of the figure shows the  
12 corresponding region 1, 2 and 3 CFADs of the single eyewall cases (Figs. 1b,d,f, respectively).  
13 The bulk of the distribution contained within the contours for frequencies  $> 50\%$  of the  
14 maximum frequency in the distribution (shading from yellow to red) is referred to below as the  
15 *modal distribution*. We refer to the frequencies that are less than 50% of the maximum frequency  
16 (green, teal, and blue contours) as the *outlier distribution*.

17 The general differences between the concentric and single eyewall cases are highlighted in  
18 Figs. 2a,b, which show the maximum reflectivity reached by the 30%, 50%, and 70% contours in  
19 the plotted CFADs below 4.5 km. In the concentric eyewall cases, the maximum reflectivity is  
20 highest in the primary eyewall (red bar, Fig. 2a) at the 30% and 50% contour interval (pale blue  
21 contour and black contour bordering yellow region, respectively, Fig. 1). At the 70% contour  
22 interval (orange contour, Fig. 1), the maximum reflectivity of the secondary eyewall (blue bar,

1 Fig. 2a) is equal to that of the primary eyewall. This result is partially predetermined by the  
2 methodology, since during case selection the secondary eyewall was required to have low-level  
3 reflectivities comparable to the eyewall. The moat maximum reflectivity (green bar, Fig. 2a) is  
4 distinctly less than either of these two regions.

5 In the single eyewall cases (Fig. 2b), the reflectivity intensity in the eyewall (red bar) is the  
6 greatest and drops off monotonically with radius for all three contour intervals. For the 30%  
7 contour, the step downward in reflectivity intensity is steep to region 2 (green bar, Fig 2b), but  
8 for the other contour intervals the decrease is less severe. This step-down in reflectivity intensity  
9 with radius in the single eyewall cases is distinctly different from the U-shaped change of  
10 reflectivity intensity with radius seen in the concentric eyewall cases (Fig 2a). This finding is  
11 again partially a result of the methodology, as mentioned above. Nevertheless, we see that the  
12 primary concentric eyewall and single eyewall share relatively similar reflectivity intensities (at  
13 the 30% and 70% contour intervals), the moat is significantly weaker in reflectivity intensity  
14 than region 2 of the single eyewall cases at all intervals, and the secondary eyewall is  
15 significantly more intense than region 3 of the single eyewall cases at all intervals. These  
16 differences in reflectivity intensity point to a difference in processes occurring in concentric  
17 versus single eyewall cases. Note that these results only apply to the precipitating pixels seen by  
18 the PR, more specifically only to reflectivities above the PR's minimal detectable threshold of  
19 ~17 dBZ. The number of precipitating pixels counted in this study, and the total number possible  
20 for all of the accumulated volumes, are listed in Table 1.

21 Figures 2c,d show the fractional areal coverage of precipitating pixels as a function of height.  
22 For a given region, the areal coverage calculation divides the total number of precipitating pixels  
23 accumulated from the overpasses at a particular altitude by the accumulated total number of

1 possible pixels. We believe that the fractional areal coverage is easier to think about than  
2 absolute area, and it also accounts for the pre-/post-boost change in pixel size mentioned in  
3 Section 2.

4 In the concentric eyewall cases, the primary eyewall displays a gradual decrease in coverage  
5 from  $\sim 1.75$  km to the melting level, and then drops off more rapidly with height above (red line,  
6 Fig. 2c). This decrease with height is primarily a signature of the slope of the eyewall as well as  
7 the subsidence in the eye affecting the inner edge of the eyewall cloud. The moat (green line, Fig  
8 2c) has an even steeper decrease in coverage with height below the melting level, with  
9 subsidence in the moat (Houze et al. 2007) being the likely reason. Also, the overall coverage is  
10 less at all levels in the moat, consistent with the precipitation coverage of the moat tending to be  
11 sparse. The secondary eyewall (blue line, Fig 2c) is unique in that the areal coverage is more  
12 constant with height below the melting level than the primary eyewall, and the secondary  
13 eyewall has significantly greater total coverage at all levels. This greater overall coverage is  
14 partially a result of the case selection, since the secondary eyewall was required to be fully  
15 circular. Above the melting level ( $\sim 5$  km), the coverage of the secondary eyewall decreases more  
16 rapidly with height than either the primary eyewall or the moat, indicating a limit to the vertical  
17 transport of particles in this region. However, these characteristics of the secondary eyewall  
18 profile point to a full reflectivity field below that limit, which indicates that a robust transport of  
19 particles was occurring vertically, radially and/or tangentially in the lower portion of the  
20 secondary eyewall.

21 In the single eyewall cases (Fig. 2), the fractional coverage is similar among the three  
22 regions. Some slight differences are, however, evident: In the low levels, region 2 (green line,  
23 Fig. 2d) has the greatest total coverage, followed by regions 3 (blue line) and 1 (eyewall; red

1 line), respectively. Because of a more gradual decrease in coverage with height, the eyewall  
2 (region 1) eventually has equal coverage to region 2 by 9 km. This change above the melting  
3 level indicates the robust vertical transport of particles within the eyewall, and the radial  
4 transport of those particles outward. The single eyewall has the same vertical characteristics as  
5 the primary concentric eyewall (red line, Fig 2c), with a decrease in coverage with height in the  
6 low levels that sharpens in upper levels. The vertical profiles of the other two regions (green,  
7 blue lines, Fig 2d) resemble those of the secondary concentric eyewall region (blue line, Fig 2c),  
8 with a more constant areal coverage below the melting level and a sharper decrease in coverage  
9 above. The higher overall areal coverage of region 2 (green line, Fig 2d), especially in the upper  
10 levels, indicates that this region is likely receiving larger and/or a greater number of particles  
11 radially from the eyewall, since otherwise the profile is identical in shape to region 3 (blue line).

12 From the above discussion, we see that in the concentric eyewall cases, the inner (dying)  
13 eyewall retains a vertical structure similar to the primary eyewall of single eyewall storms. The  
14 outer (secondary) eyewall is more robust in the sense that it has much greater fractional areal  
15 coverage at all altitudes than the inner eyewall. The rapid drop off of fractional areal coverage  
16 above 5 km in the outer eyewall suggests, however, that it also has some aspects of the structure  
17 of the non-eyewall (rainband) convection that occupies regions 2 and 3 of single eyewall cases.  
18 This result is consistent with the idea that the secondary eyewall of the concentric cases forms  
19 out of rainband material but restructures itself from the bottom up as the secondary eyewall  
20 forms. The following subsections will delve further into the region 1, 2, and 3 features of the  
21 concentric eyewall cases.

1        *a. The primary eyewall*

2        The CFAD of the primary eyewall (Fig. 1a) exhibits many characteristics in common with all  
3 tropical cyclone eyewalls, as described by Hense and Houze (2011): an intense and deep  
4 reflectivity distribution with intermittent (outlier) echoes of even greater depth and intensity. The  
5 peak of the low-level distribution occurs just below 35 dBZ, and the modal reflectivity  
6 distribution extends from ~25-44 dB. The outliers vary from minimal detectable to ~50 dB. In  
7 the upper levels, the modal distribution extends to about 9 km for 20 dBZ, but the outliers  
8 continue upward to nearly 12 km. Although the decrease in reflectivity with height in the modal  
9 distribution is rapid above the layer of melting ice, the outliers decrease more slowly with height,  
10 indicating a wide variety in the sizes and/or quantities of particles reaching high altitudes.

11        These characteristics are further drawn out by Fig. 3, which shows the mean, standard  
12 deviation, skewness, and excess kurtosis of the CFADs at every level as functions of height. The  
13 primary eyewall distribution (red lines, Figs. 3a,c,e) has a high mean, > 40 dBZ at the lowest  
14 levels, decreasing to 35 dBZ by the melting level, and decreasing further to 22 dBZ at 11 km (red  
15 line, Fig. 3a). The standard deviation is also high, being close to 10 dB at the lowest levels,  
16 slowly decreasing to about 7.5 dB by the melting level, and continuing to decrease to about 3 dB  
17 by 10 km. The entire primary eyewall distribution is negatively skewed, indicating that the bulk  
18 of the distribution is in higher reflectivities that tail towards weaker values, but this skew  
19 moderates towards a more even distribution in the upper levels (red line, Fig. 3c). The excess  
20 kurtosis is also negative at all levels, indicating a flat and shouldered distribution (red line, Fig  
21 3e). Together these moments of the distribution indicate both the strength of the overall  
22 circulation of the primary concentric eyewall and the variability in its structure with height.

1 Specifically, they indicate that the primary concentric eyewall distribution is particularly  
2 influenced by the presence of intense outliers.

3 These characteristics are similar to those seen in single eyewalls (Figs. 1b,d,f). The low-level  
4 peak of the distribution of the single eyewalls is less intense, likely because the single eyewall  
5 cases contain storms of all intensities (Category 1-5), whereas the concentric eyewall cases'  
6 storm intensities range between a strong Category 2 and a weak Category 5. The standard  
7 deviation within the single eyewall is greater and the decrease in reflectivity with height is less  
8 (red line, Fig. 3b), suggesting that suppression of the more intense convection is occurring in the  
9 primary eyewall of concentric cases, perhaps as a result of it being in a state of decline.

10 Thus, the statistics do not show a dramatic change in reflectivity structure in the primary  
11 concentric eyewall while an active secondary eyewall is in place, although the circulation is not  
12 as deep as that of a single eyewall, and it contains fewer intense outlier cells. These results  
13 suggest that while the primary eyewall is still active, it retains its basic vertical structure until it  
14 dissipates. Because of the methodology, the concentric eyewall storms are likely in a weakening  
15 phase (Sitkowski and Kossin 2011), so capturing the primary eyewall in varying phases of  
16 decline likely introduces some variability into the statistics. To test the robustness of these  
17 results, we subsampled the 166 single eyewall overpasses' Region 1 data into 1000 randomly  
18 chosen sets of 37 overpasses (same sample size as the set of concentric eyewall samples). The  
19 mean and standard deviation profiles of the primary concentric eyewall was weaker and less  
20 varied in the upper-levels than the envelope containing 999 of the 1000 means and standard  
21 deviation profiles of the subsampled single eyewall groups in the manner discussed above (Fig.  
22 4a,b). However, as shown in Hince and Houze (2011), this vertical structure is not symmetric  
23 around the entirety of the eyewall. How this structure changes around the primary eyewall, and

1 how this differs from the usual progression of reflectivity around the eyewall, will be discussed  
2 in Section 4.

3 *b. The moat*

4 As mentioned before, the moat is generally categorized by the significantly weaker and/or  
5 missing precipitation between the primary and secondary eyewall. What precipitation remains  
6 gives interesting insights into the structure of the moat. The moats in this sample varied in width  
7 between 4.5-57.5 km (not shown), with an average of ~20 km (Table 1). As seen in Fig. 1c, the  
8 low-level reflectivities are generally at least 5 dB weaker than in the primary or secondary  
9 eyewall, although some slightly more intense and deep echoes appear in the outliers.

10 Interestingly, almost all of the upper-level reflectivities came from the NW Pacific cases, with  
11 the Atlantic cases showing fewer and weaker upper-level reflectivities (not shown).

12 In contrast with the primary concentric eyewall (or the secondary), the moat distribution is  
13 marked by a comparatively low mean and standard deviation (green lines, Fig. 3a), indicating  
14 weaker and more uniform precipitation. The low-level skewness is negative, but unlike the  
15 primary eyewall the moat skewness is positive above 8 km, indicating that the upper-level  
16 reflectivities are bulked into lower intensity bins with a greater tail towards higher reflectivities  
17 (green line, Fig 3c). The excess kurtosis is also negative at low levels and positive at higher  
18 levels with a maximum at 8 km, indicating a highly peaked upper-level distribution (green line,  
19 Fig 3e).

20 These characteristics are a hallmark radar signature of stratiform precipitation, which is  
21 generally light to moderate in intensity, and horizontally and vertically uniform except for the  
22 rapid increase in reflectivity at the melting level known as the brightband (Yuter and Houze

1 1995; Houze 1997). These features result in a tightly packed, highly uniform, upper-level profile  
2 above a brightband signature in the melting layer, and a broader but still relatively uniform  
3 lower-level profile. However, unlike the stratiform precipitation seen in mesoscale convective  
4 systems, the stratiform-like precipitation seen in tropical cyclones is as likely occur as a result of  
5 ice particles being transported over large distances and slowly falling out than from local growth  
6 of particles in mesoscale updraft motion outside of the eyewall. Thus, the precipitation in the  
7 moat region seems most likely to be a combination of echoes from the primary eyewall in cases  
8 where the primary eyewall was not entirely circular, transport of ice particles outward by the  
9 primary eyewall circulation, and local relatively weak convection that has not been completely  
10 suppressed.

### 11 *c. The secondary eyewall*

12 Given that the cases selected were required to have both a primary and secondary eyewall,  
13 the vertical structure described here refers to the developing secondary eyewall that has formed  
14 but not taken over as the primary eyewall. We see that the secondary eyewall at this stage has a  
15 vertical structure unlike that of either the primary concentric eyewall or of the single eyewall in  
16 non-concentric-eyewall cases. It seems reasonable to conjecture that the secondary eyewall's  
17 vertical structure becomes that of a single eyewall storm once the primary eyewall has fully  
18 dissipated and its radial outflow no longer confines the secondary eyewall to lower levels.

19 What makes the secondary concentric eyewall unique at the intermediate stage investigated  
20 here is its uniformity and intensity, as seen in Fig. 1e. The low-level modal distribution spans  
21 only 10 dB, compared to 15-20 dB in the primary concentric eyewall and 20 dB in the single  
22 eyewall (cf. Figs. 1a,b). The vertical extents of the echoes are relatively modest compared to the

1 other two eyewalls, with the modal distribution reaching ~9 km and the outliers reaching 10.5  
2 km. The outliers are much more compressed around the modal distribution at all levels, which is  
3 distinctly different from either of the other two kinds of eyewalls.

4 The most distinct difference in the secondary eyewall distribution is that this distribution is  
5 tightly centered on relatively high reflectivity values of 35-37 dB. Note the relative absence of  
6 lower tropospheric reflectivity values  $< \sim 30$  dBZ. *This combination of intensity and annular*  
7 *uniformity is not seen anywhere else within a tropical cyclone.* This type of distribution does not  
8 occur in any primary or single eyewall: a Category 4-5 single eyewall has that intensity (or  
9 greater) but not the uniformity, and storms located over marginal sea surface temperatures tend  
10 towards that uniformity but not that intensity (see Hense and Houze 2011 for details). As seen in  
11 Fig. 1d,f, the regions just outside of the single eyewall (i.e. rainbands) have high upper-level  
12 uniformity in their distribution, indicating large quantities of ice. The less uniform lower-level  
13 distribution in the rainband regions indicates a wider range of light to moderate rain. A pinching  
14 of the rainband CFADs just above the melting layer suggests a distinct particle regime change  
15 between the upper and lower layers of the rainband regions, which is distinctly unlike the  
16 smoother transition seen in the single-eyewall CFAD (Fig. 1b). The region 2 CFAD of the single  
17 eyewall cases (Fig. 1d) in particular has some intense outliers and some echo heights reaching  
18 11.5 km, likely resulting from upper-level transport of particles from the eyewall as well as the  
19 intermittent presence of intense convective cells. Except for the highly intense and uniform low-  
20 level reflectivities, the secondary concentric eyewall CFAD above the melting level shares these  
21 characteristics with the region 2 and region 3 CFADs. Comparing the secondary concentric  
22 eyewall CFAD to the rainband CFADs of the single eyewall cases suggests that the secondary  
23 eyewall still has some rainband-like characteristics, but that processes occurring at lower levels

1 are intensifying the precipitation, pulling the lower-tropospheric reflectivity distribution over to  
2 more intense reflectivities.

3 The statistics calculated on the secondary eyewall distribution (blue lines, Fig. 3a,c,e)  
4 highlight these differences. The low-level mean reflectivity of the secondary eyewall (expressed  
5 as dBZ; blue line, Fig. 3a) is comparable to that of the primary eyewall, but the upper-level mean  
6 reflectivity is like that of the moat, suggesting that the secondary eyewall has an intense  
7 circulation that is vertically suppressed. The standard deviation is lower than even that of the  
8 moat in low levels but is the same in upper levels (blue line, Fig. 3a). Below 5 km, the secondary  
9 eyewall is the most negatively skewed of the three regions, showing the greater tendency of the  
10 distribution to be bulked in the higher reflectivity bins, but like the moat and the rainbands of the  
11 single eyewall cases, the skewness becomes positive at about 7 km, again showing similarity to  
12 the rainbands at upper levels, with the tendency to be evenly distributed at higher levels  
13 (compare the blue lines in Figs. 3c,d).

14 The excess kurtosis is positive above 7 km (blue line, Fig. 3e). Because of the large amounts  
15 of small ice particles circulating around the storm (Black and Hallett 1986, 1991), a peaked  
16 upper-level distribution (positive excess kurtosis) and a brightband are ubiquitous features  
17 anywhere outside of the eyewall. The excess kurtosis dips negative in the melting layer,  
18 representing the above-noted pinching that separates the lower tropospheric CFAD portion from  
19 that just above the melting layer, indicating very different distributions in the lower and upper  
20 troposphere of the secondary concentric eyewall. These characteristics are again similar to the  
21 excess kurtosis profiles of regions 2 and 3 of the single eyewall cases (green, blue lines, Fig. 3f).  
22 However, the excess kurtosis of the outer concentric eyewall is especially unique because this  
23 distribution is the only one in the entire study that has a positive kurtosis at low levels, indicating

1 a highly peaked, heavily tailed profile (blue line, Fig. 3e). This change in the excess kurtosis is a  
2 signature of the tightening in the low-level reflectivity distribution of the secondary eyewall  
3 toward higher reflectivities seen in the CFADs. The rainband CFADs, in contrast, are nearly  
4 identical in excess kurtosis to the secondary eyewall at the negative peak at 6 km, but only  
5 become less negative instead of gaining a positive value at lower levels (Fig. 3f), indicating the  
6 more variable distribution in the lower troposphere compared to the developing secondary  
7 concentric eyewall.

8 To summarize, at and above the melting layer, the secondary concentric eyewall shares many  
9 of the statistical details of regions 2 and 3 (rainband regions) of the single eyewall cases,  
10 suggesting that the secondary concentric eyewall is formed from rainband material. The  
11 robustness of these results was born out by subsampling the 166 single eyewall overpasses'  
12 Region 2 data into 1000 randomly chosen sets of 37 overpasses. The mean and standard  
13 deviation profiles of the secondary concentric eyewall are weaker in the upper-levels, more  
14 intense in the low levels, and less varied at all levels than all of the possible means and standard  
15 deviation profiles of the subsampled single eyewall Region 2 groups (Figs. 4c,d). Even in low  
16 levels, the general shape of the vertical profiles of statistics of the radar echoes in the secondary  
17 concentric eyewall are a shifted version of the rainband statistics, while the primary concentric  
18 eyewalls and single eyewalls have distinctly different characteristics. The intensity and  
19 uniformity of the lower-tropospheric reflectivity distribution shows that the burgeoning  
20 secondary circulation forming within the secondary eyewall is generating precipitation at  
21 eyewall-like intensities, which is greater than what is typically seen at this radius. This  
22 developing circulation, however, is evidently vertically restricted to mostly occurring below the  
23 melting layer, as at upper levels little difference is seen between the secondary concentric

1 eyewalls and the rainbands of single eyewall storms. The lower-tropospheric uniformity of the  
2 secondary eyewall distribution suggests that axisymmetrization is beginning to help the  
3 developing secondary concentric eyewall to coalesce at lower levels. As will be discussed in the  
4 next section, the secondary eyewall is highly symmetric at this stage in its development,  
5 suggesting an azimuthal uniformity of processes in low levels.

#### 6 **4. Quadrant-by-quadrant variations in the three eyewall types**

7 The statistics discussed above show that the primary and secondary concentric eyewalls have  
8 important differences in structure that suggest how the overall processes that may be governing  
9 their circulations differ from those in a single-eyewall storm. Like single eyewall cases,  
10 concentric eyewalls are often not fully symmetric in reflectivity structure; however, as will be  
11 shown below, the primary and secondary concentric eyewalls differ from both each other and  
12 from single eyewalls.

##### 13 *a. Shear effects on the inner eyewall of concentric eyewall storms in comparison to single* 14 *eyewall cases*

15 This section examines how the shear-relative asymmetric structure of the primary concentric  
16 eyewall compares to the asymmetry seen in single eyewall storms. Hence and Houze (2011)  
17 found that although the single eyewall is highly resilient in structure with respect to shear,  
18 CFADs show a progression of small differences of reflectivity vertical structure around the  
19 single eyewall, most likely related to the progression of shear-induced variation in location of  
20 convective cell initiation around the eyewall (Fig. 5 of Hence and Houze 2011). The general  
21 characteristics of this progression are apparent in Figs. 5a,b, which include the fractional areal  
22 coverage, mean, and standard deviation of the single eyewall quadrant-by-quadrant CFADs (not

1 shown) as seen in this study's expanded dataset. The low-level means and standard deviations of  
2 reflectivity are nearly identical in all quadrants relative to the shear vector (Fig. 5b). The  
3 fractional areal coverage indicates how the bulk of the precipitation (as indicated by the lower-  
4 tropospheric reflectivity) is deposited in the downshear-left (DL, black lines) quadrant at all  
5 levels, and the least in the upshear-right (UR, orange lines) quadrant (Fig. 5a). The upshear-left  
6 (UL, teal lines) quadrant has the highest upper-level mean and standard deviation, followed by  
7 the upshear-right (UR, magenta lines), with lower values found downshear.

8 As discussed by Hencé and Houze (2011), these features, combined with the broadening of  
9 the upper-level modal distribution in the DR CFAD (not shown), suggest that the convective  
10 cells began their life in the DR quadrant. These cells grow and intensify in the DL quadrant,  
11 generating large particles with high reflectivity, but begin to weaken in the UL quadrant before  
12 dissipating in the UR quadrant. This process exaggerates with increasing shear, as the NW  
13 Pacific single eyewall cases have a somewhat greater left-of-shear asymmetry than the Atlantic  
14 single eyewall cases, with the formation region pushing more into the DL quadrant (average  
15 shear magnitude 9.8 vs. 8.5  $\text{m s}^{-1}$  [per 850 hPa-200 hPa], respectively; not shown). The smaller  
16 ice particles that are lofted to upper levels by the intense convection in the DL are quickly  
17 transported to appear as more intense upper-level reflectivities in the UL. These weak high-  
18 altitude echoes gradually lower in height and weaken in intensity as they travel to UR and DR  
19 quadrants. These results are consistent with the inferences of Black et al. (2002), who concluded  
20 that the upper-level exhaust of shear-induced convective cells mostly covered the upshear  
21 quadrants. Marks and Houze (1987) found that smaller ice particles that reach the eyewall  
22 outflow can stay aloft for 1-2 h, and at eyewall tangential velocities they can thus circulate up to  
23 1.5 times around the eyewall. We suggest that while the larger particles are falling out primarily

1 in the DL and UL, the smaller ice particles generated in the DL can fall out in any quadrant, but  
2 register at lower and lower altitudes as they progress downwind.

3 These general features of the single eyewall exaggerate climatologically in the primary  
4 eyewall of a concentric eyewall storm. Fig. 5c shows how the precipitation is strongly favoring  
5 the left-of-shear side of the primary concentric eyewall, expressed by greater fractional areal  
6 coverage in the left-of-shear quadrants. The low-level means and standard deviations also divide  
7 along the shear vector, with the left-of-shear side being more intense ( $\sim 3\text{-}4$  dB) and variable than  
8 the right-of-shear side (Fig. 5d). This division by shear is more pronounced than in the single  
9 eyewall storms (cf. Fig. 5a,b), suggesting perhaps that the weakening inner eyewall of a storm  
10 undergoing eyewall replacement is more susceptible to shear induced asymmetry than is a robust  
11 single eyewall not being affected by eyewall replacement. This susceptibility occurs even though  
12 the average shear magnitude of concentric eyewall cases is lower than in the single eyewall cases  
13 (Table 1). The individual basins again further illustrate this tendency, since the Atlantic primary  
14 eyewalls are significantly more asymmetric in coverage and intensity than single eyewalls with  
15 similar average shear magnitudes (average shear magnitude  $8.40$  vs.  $8.49$   $\text{m s}^{-1}$  [per 850 hPa-200  
16 hPa], respectively; not shown). The NW Pacific primary eyewalls are also more asymmetric in  
17 fractional areal coverage, although similar in intensity, to their single eyewall counterparts, with  
18 the average shear magnitude being lower ( $6.99$  vs.  $9.77$   $\text{m s}^{-1}$  [per 850 hPa-200 hPa] respectively;  
19 not shown).

20 The CFADs for quadrants of the primary concentric eyewall cases (not shown) are similar in  
21 quadrant progression to what was described for the single eyewall, although the right-of-shear  
22 quadrants' outliers are more strongly suppressed, suggesting that the convection formation  
23 region may have shifted more into the DL. This asymmetry shifts above the melting level with

1 the more intense reflectivities being in the upshear quadrants (Fig. 5d), again suggesting that the  
2 upshear quadrants are receiving the lofted ice particles from the intense convection in the left-of-  
3 shear quadrants. The enhanced convection asymmetry within the primary concentric eyewall  
4 may explain why the upper-level upshear asymmetry is more pronounced than what is seen in  
5 single eyewall cases. These general results are consistent with those seen by Franklin et al.  
6 (1993) in Hurricane Gloria (1985), who found that as in single eyewall storms, environmental  
7 vertical wind shear influenced the distribution of convection around the eyewall.

8 *b. Shear effects on the outer eyewall of concentric eyewall storms and comparison to the*  
9 *inner eyewall*

10 The lower-tropospheric echo intensity in the secondary concentric eyewall is greater in the  
11 left-of-shear quadrants (Fig. 5f). However, unlike the primary concentric eyewall, this difference  
12 is only about 1 dB and only extends to the melting level—above that, the mean reflectivity is  
13 nearly identical in all quadrants. The standard deviation is also highly similar at all levels. The  
14 main asymmetry appears in the fractional areal coverage, which is generally larger to the left of  
15 shear (Fig. 5e). These differences between the left and right of shear indicate the nature of the  
16 wavenumber-1 asymmetry in the reflectivity distribution of the secondary eyewall: the left-of-  
17 shear quadrants are slightly more intense than the right-of-shear quadrants and have somewhat  
18 more echo coverage. However, there is no indication of a quadrant-to-quadrant progression in  
19 the nature of the convection, since the convection in all quadrants appears to be of a similar  
20 character. Rather, the convective cells apparently develop in the convectively favored left-of-  
21 shear quadrants and are able to develop into slightly stronger and more intense cells, but these  
22 cells seem to mostly grow and die close to their originating quadrant. Convection on the

1 convectively disfavored side of the secondary eyewall develops but does not reach quite the  
2 same intensity. Since the outer eyewall has a much greater diameter and lower tangential wind  
3 speeds than the primary concentric eyewall, it is more difficult for particles to be advected  
4 circumferentially to a different quadrant of the storm. The right-of-shear quadrants are too far  
5 away to receive particles generated in the left-of-shear quadrants, so it is likely that their  
6 reflectivity distribution is locally generated.

7 It is interesting that the secondary concentric eyewall exhibits such a comparatively small  
8 asymmetry in convective intensity even though, as noted in the previous subsection, the primary  
9 concentric eyewall exhibits an exaggerated version of what is seen in the shear-induced  
10 asymmetry of a single eyewall. One possibility is that the primary eyewall is not directly exposed  
11 to the large-scale environmental wind shear, and the moat subsidence enhances the shear-  
12 induced subsidence effect on the primary concentric eyewall in the upshear quadrants. This  
13 explanation would be consistent with the primary concentric eyewall convection being vertically  
14 suppressed compared to single eyewall convection (compare Figs. 5b,d). The primary concentric  
15 eyewall would then have less ability to combat the shear-induced asymmetry. Another possibility  
16 is that the moat subsidence is asymmetric, as evidenced by the moat tending to contain more  
17 precipitation in the left-of-shear quadrants than the right (not shown). However, weakened  
18 subsidence in the DL moat where the convection in both the primary and secondary eyewall is  
19 most intense seems dynamically inconsistent. More likely, this imperfect moat clearing results  
20 from the enhanced particle transport or imperfect boundaries mentioned above. Yet another  
21 possibility is that the secondary concentric eyewall's influence on the radial inflow is somehow  
22 asymmetric. This explanation seems somewhat unlikely because the enhanced side of the  
23 secondary concentric eyewall does not correspond to the depressed side of the primary eyewall,

1 and the overall features of the secondary eyewall are much more symmetric than the primary  
2 eyewall. In other words, convection in the secondary eyewall must be rather axisymmetric in  
3 order to have a complete eyewall, otherwise no hydrometeors would exist to create surface  
4 precipitation all the way around the storm. Modeling and Doppler analysis will be required to  
5 test these ideas.

6 *c. Schematic of the typical echo pattern of concentric eyewalls relative to the environmental*  
7 *shear*

8 Figures 6 and 7 illustrate schematically the typical structure of concentric eyewalls that can  
9 be gleaned from Fig. 5 and other figures in this paper. Figure 6 illustrates the differences in  
10 horizontal reflectivity distribution between the primary and secondary concentric eyewalls. A  
11 mostly precipitation-free moat is shown between the two eyewalls, and the sizes of the features  
12 are directly proportional to the average eye diameter and primary eyewall, moat, and secondary  
13 eyewall widths listed in Table 1. The inner edges of the two eyewalls are concentric, but the  
14 outer edges vary in width, related to the fraction of areal coverage shown in Fig. 5. The quadrant  
15 with the maximum areal coverage is shown to have the maximum area for that quadrant; the  
16 other quadrants are sized downward respectively. The bulk of the precipitation in the primary  
17 eyewall, both in amount and intensity, are weighted to the downshear-left side, with the upshear-  
18 right quadrant exhibiting a minimum in both, consistent with Fig. 5c. As hypothesized in Section  
19 4a, the convective cells are shown beginning their development in the downshear-right quadrant,  
20 growing and intensifying in the downshear-left quadrant, and becoming weaker in the upshear-  
21 left quadrant, before dissipating entirely in the upshear-right quadrant. The bulking of the  
22 precipitation in the downshear-left quadrant of the primary eyewall results in a narrowing of the

1 moat in that quadrant, whereas the moat in the upshear-right quadrant is wider and clearer. As  
2 inferred from Figs. 5e,f, the secondary eyewall also exhibits a wavenumber-1 asymmetry in  
3 convective intensity. The upshear-left quadrant has the fullest reflectivity field, but the  
4 precipitation is most intense in the downshear-left quadrant. As hypothesized in Section 4b from  
5 Figs. 5e,f we speculate that convective cells overall generate and disperse more locally than  
6 those in the primary eyewall.

7 Figure 6 also illustrates some idealized particle trajectories inferred from Fig. 5c-f. These  
8 trajectories are estimated as in Marks and Houze (1987) and using the azimuthal average low-  
9 level winds from Didlake and Houze (2011). With the Marks and Houze (1987) calculation that  
10 the larger eyewall particles take about 10 min to fall, this would generously assume that the  
11 particles would fall within 36 km in the primary eyewall (travelling at  $60 \text{ m s}^{-1}$ , or Category 4  
12 intensity) or 30 km in the outer eyewall (travelling at  $50 \text{ m s}^{-1}$ ). As shown in Fig. 6, a large  
13 particle could travel from its generation almost a full quadrant in the primary eyewall, but  
14 because of the large distances in the secondary eyewall a similar particle would only cover a  
15 quarter of the downshear-left quadrant. A smaller eyewall particle took 1-2 hours to fall out in  
16 Marks and Houze (1987). At the same wind speeds, this smaller particle could travel up to 324  
17 km in the primary eyewall and 270 km in the secondary eyewall. As shown in Figure 6, this  
18 translates to a more than complete circuit in the primary eyewall, but less than half a circuit in  
19 the secondary eyewall. These differences in transit distances likely explain the differences in  
20 horizontal precipitation distribution between the primary and secondary eyewalls.

21 Figure 7 idealizes a cross-section through the strongest and weakest portions of the  
22 concentric eyewalls along line AB in Fig. 6. Consistent with Figs. 5c,d, the left-of-shear side A  
23 exhibits more intense convection, with high reflectivities reaching higher heights in the primary

1 eyewall. We speculate that the enhanced convection on this side of the primary eyewall would  
2 intensify transport of precipitation particles outwards, which would narrow and shorten the moat.  
3 As inferred from Figs. 5e,f, convection in this portion of the secondary eyewall is nearly as  
4 intense but not quite as tall as the primary. The lack of higher upper-level reflectivities could be a  
5 combination of enhanced vertical suppression from the primary eyewall as well as enhanced  
6 transport of the smaller precipitation particles downwind. On the right-of-shear side B, the  
7 precipitation at all but the uppermost levels and at all radii is lighter (consistent with Figs. 5d,f).  
8 The primary eyewall, likely receiving its precipitation from upwind, is shown to be narrower and  
9 significantly less intense. As inferred from Fig. 5d, this downwind particle transport is shown to  
10 appear especially in the upper levels of the primary eyewall, which have a greater tendency  
11 towards higher reflectivities. With a weakened convection in this part of the primary eyewall, the  
12 moat is shown to be wider and taller. Consistent with Fig. 5f, the secondary eyewall's convection  
13 on this side is weaker but still present and active, and is much more similar to its left-of-shear  
14 counterpart than the asymmetry seen in the primary eyewall.

## 15 **5. Conclusions**

16 Statistical analysis of TRMM PR three-dimensional data collected over 10 years reveals that  
17 the secondary (outer) eyewalls of concentric eyewall tropical cyclones exhibit departures in  
18 structure from the eyewalls of single eyewall storms and are also different from the primary  
19 (inner) eyewall precipitation structure of concentric eyewall storms. The inner eyewalls maintain  
20 a deep (high-altitude) and intense (high-reflectivity) mean structure, similar to the structure  
21 described for single eyewalls by Hance and Houze (2011), while they remain active, although  
22 they are somewhat less deep than the eyewalls of single eyewall storms. The inner concentric

1 eyewalls are more susceptible to shear asymmetry than are the eyewalls of single eyewall storms.  
2 What precipitation exists in the moat is light in intensity and vertically limited. The secondary  
3 (outer) concentric eyewall is nearly as intense as the inner eyewall in low levels but it is less  
4 deep than the inner eyewall. The secondary eyewall's precipitation is more intense through the  
5 lower troposphere than is precipitation seen at the same radius in single eyewall storms.

6 The secondary concentric eyewalls examined in this study have formed but not yet replaced  
7 the inner eyewalls. At this intermediate stage of development, the secondary eyewalls resemble  
8 rainbands in their upper levels and eyewalls in their lower levels. The secondary eyewall has the  
9 same highly uniform upper-level distribution and melting signature as the rainbands, indicating a  
10 separate ice-particle distribution aloft than what is being generated in low levels. However,  
11 unlike rainbands, the low-level distribution of the secondary eyewall is both highly uniform and  
12 intense. This combination of upper- and lower-level features is completely unique to the  
13 secondary concentric eyewalls. The high intensity and great uniformity in the low levels, but  
14 rainband-like distribution of reflectivity in the upper levels, suggests that the secondary eyewall  
15 is largely made of rainband material that is undergoing modification to form a circular eyewall  
16 feature, and that the convective processes creating this new eyewall are building it from below.  
17 These convective processes also seem to be highly resistant to environmental vertical wind shear,  
18 with the left-of-shear side being only marginally favored for more intense convection with  
19 increasing shear.

20 Future work will expand this type of analysis to the rainband region of the storm, i. e. the  
21 region lying radially outside the eyewall regions of both single and concentric eyewall storms.  
22 This work could also be explored using the global TRMM dataset and possibly including  
23 lightning data from the TRMM Lightning Sensor (LIS) or other lightning networks. The ideas

1 germinated in these statistical studies will need to be examined in the context of high-resolution  
2 models resolving the convective-scale substructure of precipitating clouds of tropical cyclones.

3 *Acknowledgments:* Tia Lerud assisted with case identification, database creation and analysis.

4 We are grateful to Anthony Didlake and Stacy Brodzik for help and comments. Beth Tully

5 provided graphics and editing support. NCEP Reanalysis data provided by the

6 NOAA/OAR/ESRL PSD, Boulder, Colorado, USA (<http://www.esrl.noaa.gov/psd/>). This

7 research was sponsored by NSF RAINEX grants ATM-0432623 and ATM-0743180, NASA

8 PMM grants NAG5-13654, NNX07AD59G and NNX10AH70G, NASA Earth and Space

9 Science Fellowship NNX06AF17H, and a NASA Space Grant Fellowship.

## REFERENCES

- Awaka, J., T. Iguchi, and K. Okamoto, 2009: TRMM PR standard algorithm 2A23 and its performance on bright band detection. *J. Meteo. Soc. Japan*, **87A**, 31-52.
- Black, M. L., and H. E. Willoughby, 1992: The concentric eyewall cycle of Hurricane Gilbert. *Mon. Wea. Rev.*, **120**, 947-957.
- Black, M. L., J. F. Gamache, F. D. Marks, C. E. Samsury, and H. E. Willoughby, 2002: Eastern Pacific Hurricanes Jimena of 1991 and Olivia of 1994: The effect of vertical shear on structure and intensity. *Mon. Wea. Rev.*, **130**, 2291-2312.
- Black, P. G., H. V. Senn, and C. L. Courtright, 1972: Airborne radar observations of eye configuration changes, bright band distribution, and precipitation tilt during the 1969 multiple seeding experiments in Hurricane Debbie. *Mon. Wea. Rev.*, **100**, 208-217.
- Black, R. A., and J. Hallett, 1986: Observations of the distribution of ice in hurricanes. *J. Atmos. Sci.*, **43**, 802-822.
- Bluestein, H. B., and F. D. Marks, 1987: On the structure of the eyewall of Hurricane Diana (1984): comparison of radar and visual characteristics. *Mon. Wea. Rev.*, **115**, 2542-2552.
- Chen, S. Y. S., J. A. Knaff, and F. D. Marks, 2006: Effects of vertical wind shear and storm motion on tropical cyclone rainfall asymmetries deduced from TRMM. *Mon. Wea. Rev.* **134**, 3190-3208.
- Corbet, J., C. Mueller, C. Burghart, K. Gould, and G. Granger, 1994: ZEB - Software for the integration, display, and management of diverse environmental datasets. *Bull. Amer. Meteor. Soc.*, **75**, 783-792.
- DeCarlo, L.T., 1997: On the meaning and use of kurtosis. *Psychological Methods*, **2**, 292-307.

- Didlake, A. C., Jr., and R. A. Houze, Jr., 2011: Kinematics of the secondary eyewall observed in Hurricane Rita (2005). *J. Atmos. Sci.*, **68**, 1620-1636.
- Dodge, P., R. W. Burpee, and F. D. Marks, 1999: The kinematic structure of a hurricane with sea level pressure less than 900 mb. *Mon. Wea. Rev.*, **127**, 987-1004.
- Franklin, J. L., S. J. Lord, S. E. Feuer, and F. D. Marks, 1993: The kinematic structure of Hurricane Gloria (1985) determined from nested analyses of dropwindsonde and Doppler radar data. *Mon. Wea. Rev.*, **121**, 2433-2451.
- Hence, D. A., and R. A. Houze, Jr., 2011: Vertical structure of hurricane eyewalls as seen by the TRMM Precipitation Radar. *J. Atmos. Sci.*, **68**, 1637-1652.
- Houze, R. A., Jr., 1997: Stratiform precipitation in regions of convection: A meteorological paradox? *Bull. Amer. Meteor. Soc.*, **78**, 2179-2196.
- , 2010: Clouds in Tropical Cyclones. *Mon. Wea. Rev.*, **138**, 293–344.
- Houze, R. A., Jr., D. C. Wilton, and B. F. Smull, 2007: Monsoon convection in the Himalayan region as seen by the TRMM Precipitation Radar. *Quart. J. Roy. Meteor. Soc.*, **133**, 1389-1411.
- Houze, R. A., Jr., S. S. Chen, B. F. Smull, W. C. Lee, and M. M. Bell, 2007: Hurricane intensity and eyewall replacement. *Science*, **315**, 1235-1239.
- James, C. N., S. R. Brodzik, H. Edmon, R. A. Houze, Jr., and S. E. Yuter, 2000: Radar data processing and visualization over complex terrain. *Wea. Forecasting*, **15**, 327-338.
- Jordan, C. L., 1958: Mean soundings for the West-Indies area. *J. Meteo.*, **15**, 91-97.
- Judt, F., S. S. Chen, 2010: Convectively generated potential vorticity in rainbands and formation of the secondary eyewall in Hurricane Rita of 2005. *J. Atmos. Sci.*, **67**, 3581–3599, doi: 10.1175/2010JAS3471.1.

- Kalnay et al., 1996: The NCEP/NCAR 40-year reanalysis project, *Bull. Amer. Meteor. Soc.*, **77**, 437-470.
- Knapp, K. R., M. C. Kruk, D. H. Levinson, H. J. Diamond, and C. J. Neumann, 2010: The International Best Track Archive for Climate Stewardship (IBTrACS). *Bull. Amer. Meteor. Soc.*, **91**, 363-376.
- Kossin, J. P., W. H. Schubert, and M. T. Montgomery, 2000: Unstable interactions between a hurricane's primary eyewall and a secondary ring of enhanced vorticity. *J. Atmos. Sci.*, **57**, 3893-3917.
- Kummerow, C., W. Barnes, T. Kozu, J. Shiue, and J. Simpson, 1998: The Tropical Rainfall Measuring Mission (TRMM) sensor package. *J. Atmos. Oceanic Technol.* **15**, 809-817.
- Kuo, H.-C., C.-P. Chang, Y.-T. Yang, and H.-J. Jiang, 2009: Western North Pacific typhoons with concentric eyewalls. *Mon. Wea. Rev.*, **137**, 3758-3770.
- Marks, F. D., and R. A. Houze, Jr., 1987: Inner core structure of Hurricane Alicia from airborne Doppler radar observations. *J. Atmos. Sci.*, **44**, 1296-1317.
- Qiu, X., Z.-M. Tan, and Q. Xiao, 2010: The roles of vortex Rossby waves in hurricane secondary eyewall formation. *Mon. Wea. Rev.*, **138**, 2092-2109.
- Rozoff, C. M., W. H. Schubert, and J. P. Kossin, 2008: Some dynamical aspects of tropical cyclone concentric eyewalls. *Quart. J. Roy. Meteor. Soc.*, **134**, 583-593.
- Rozoff, C. M., W. H. Schubert, B. D. McNoldy, and J. P. Kossin, 2006: Rapid filamentation zones in intense tropical cyclones. *J. Atmos. Sci.*, **63**, 325-340.
- Saffir, H. S., 2003: Communicating damage potentials and minimizing hurricane damage. Hurricane! Coping with Disaster, R. Simpson, Ed., AGU, 155-164.

- Shapiro, L. J., and H. E. Willoughby, 1982: The response of balanced hurricanes to local sources of heat and momentum. *J. Atmos. Sci.*, **39**, 378-394.
- Terwey, W. D., and M. T. Montgomery, 2008: Secondary eyewall formation in two idealized, full-physics modeled hurricanes. *J. Geophys. Res.*, **113**, D12112.
- TSDIS, 2007: Interface control specification between the Tropical Rainfall Measuring Mission Science Data and Information System (TSDIS) and the TSDIS Science User (TSU), Volume 4: File Specifications for TRMM Products - Levels 2 and 3. N. G. S. F. Center, Ed., 102.
- Willoughby, H. E., 1988: The dynamics of the tropical cyclone core. *Aust. Met. Mag.*, **36**, 183-191.
- , 1990: Temporal changes of the primary circulation in tropical cyclones. *J. Atmos. Sci.*, **47**, 242-264.
- Willoughby, H. E., J. A. Clos, and M. G. Shoreibah, 1982: Concentric eye walls, secondary wind maxima, and the evolution of the hurricane vortex. *J. Atmos. Sci.*, **39**, 395-411.
- Willoughby, H. E., F. D. Marks, and R. J. Feinberg, 1984: Stationary and moving convective bands in hurricanes. *J. Atmos. Sci.*, **41**, 3189-3211.
- Yuter, S. E., and R. A. Houze, Jr., 1995: 3-Dimensional kinematic and microphysical evolution of Florida cumulonimbus. 2. Frequency-distributions of vertical velocity, reflectivity, and differential reflectivity. *Mon. Wea. Rev.*, **123**, 1941-1963.

## FIGURE CAPTIONS

**Figure 1.** CFADs of TRMM PR reflectivity data for all of the 1998-2007 overpasses of storms that ultimately reached Category 4 or 5 intensity, for the total points of: a) region 1 (primary eyewall) of concentric eyewall cases; b) region 1 (single eyewall) of single eyewall cases; c) region 2 (moat) of concentric eyewall cases; d) region 2 of single eyewall cases; e) region 3 (secondary eyewall) of concentric eyewall cases; and f) region 3 of single eyewall cases.

Contours represent the frequency of occurrence relative to the maximum absolute frequency in the data sample represented in the CFAD, contoured every 5%. Altitudes are geopotential height (km AMSL) relative to the ellipsoidal surface of the earth. The ordinate of the CFAD is altitude (in 250 m increments, or bins) and the abscissa is reflectivity in dBZ (in 1 dB bins). The 8 km and 25 dBZ levels are indicated by the black solid lines, and the 5 km and 35 dBZ levels are indicated by the black dotted lines for ease of reference. The 20%, 50%, and 80% contours are in black for reference.

**Figure 2.** a) Maximum reflectivity reached below 4.5 km by the 30%, 50%, and 70% contours of the region 1 (primary eyewall, red bars), 2 (moat, green bars), and 3 (secondary eyewall, blue bars) concentric eyewall CFADs from Fig. 1a,c,e. b) Same as in a), but for the region 1 (single eyewall, red bars), 2 (green bars), and 3 (blue bars) single eyewall CFADs from Fig. 1b,d,f. c) Fractional areal coverage of accumulated reflectivity pixels as a function of height for region 1 (primary eyewall, red line), 2 (moat, green line), and 3 (secondary eyewall, blue line) of the concentric eyewall cases. d) Same as in c), but for region 1 (single eyewall, red line), 2 (green line), and 3 (blue line) of the single eyewall cases.

**Figure 3.** a) Mean reflectivity (solid lines) and standard deviation (dashed lines) as a function of height of region 1 (primary eyewall, red line), region 2 (moat, green line), and region 3 (secondary eyewall, blue lines) concentric eyewall CFADs. b) same as in a), but for the region 1 (single eyewall, red line), region 2 (green line), and region 3 (blue lines) single eyewall CFADs. c) Skewness as a function of height of region 1 (primary eyewall, red line), region 2 (moat, green line), and region 3 (secondary eyewall, blue lines) concentric eyewall CFADs. d) same as in c), but for the region 1 (single eyewall, red line), region 2 (green line), and region 3 (blue lines) single eyewall CFADs. e) Excess kurtosis as a function of height of region 1 (primary eyewall, red line), region 2 (moat, green line), and region 3 (secondary eyewall, blue lines) concentric eyewall CFADs. f) same as in e), but for the region 1 (single eyewall, red line), region 2 (green line), and region 3 (blue lines) single eyewall CFADs.

**Figure 4.** a) Mean reflectivity as a function of height of the total sample of the single eyewall (region 1, single eyewall cases), primary eyewall (region 1, concentric eyewall cases), and the secondary eyewall (region 3, concentric eyewall cases), with 1000 randomly chosen subsamples of the single eyewall region 1 data (black lines). b) Same as a), but for standard deviation. c) Mean reflectivity as a function of height of the total sample of region 2 of the single eyewall cases and the secondary eyewall (region 3, concentric eyewall cases), with 1000 randomly chosen subsamples of the single eyewall region 2 data (black lines). d) Same as in c), but for standard deviation.

**Figure 5.** a) Percent of areal coverage of accumulated reflectivity pixels as a function of height for the downshear-left (black line), upshear-left (teal line), upshear-right (orange line), and downshear-right (magenta line) for the single eyewall cases (region 1, single eyewall cases). b) same as in a), but for the mean reflectivity (solid) and standard deviation (dash). c) same as in a), but for the primary eyewall (region 1, concentric eyewall cases). d) same as in c), but for the mean reflectivity (solid) and standard deviation (dash). e) Same as in a), but for the secondary eyewall (region 3, concentric eyewall cases). f) same as in e), but for the mean reflectivity (solid) and standard deviation (dash).

**Figure 6.** Idealized plan-view radar signature of the inner core of a tropical cyclone exhibiting concentric eyewalls overlaid with idealized particle trajectories. The shading represents radar reflectivity at intervals of 30, 35, 37.5, 40, and 45 dBZ. The small hurricane symbol represents the center of the cyclone. The first reflectivity ring represents the primary eyewall (region 1). The size of the convective cells indicates the level of maturity, with the dashed border indicating collapsing cells. The reflectivity-free region between the two eyewall features represents the moat (region 2). The outer reflectivity ring represents the secondary eyewall (region 3). The white curled lines represent the particle path, with the symbol representing where the particle would reach the surface. The dashed arrow represents the environmental shear vector. Line AB is a cross-section idealized in Fig. 7.

**Figure 7.** Idealized vertical cross-section along line AB of Fig. 6. Scalloped region represents the cloud boundary of the convective features. The shading represents radar reflectivity at intervals of 25, 30, 35, 37.5, 40, and 45 dBZ.

## LIST OF TABLES

Table 1. Listing of the average shear, eye diameter, and region width as well as the number of accumulated precipitating pixels, number of possible pixels in the accumulated volume and the convective fraction for region 1 (primary eyewall), region 2 (moat), and region 3 (secondary eyewall) of the concentric cases as well as region 1 (single eyewall), region 2 and region 3 of the single eyewall cases.

	Concentric Eyewalls	Single Eyewall
Number of Cases	37	371 (164 eyewall data)
Average shear magnitude	7.6 m s <sup>-1</sup> per (850 hPa – 200 hPa)	9.1 m s <sup>-1</sup> per (850 hPa – 200 hPa)
Average Eye Diameter	40.74 km	45.95 km
R1 average width	26.26 km	17 km
R1 Precipitating pixels in Volume	81991	258310
R1 Possible Pixels in Volume	570090	2759557
R2 average width	20.14 km	39.98 km
R2 Precipitating pixels in Volume	66853	1541318

R2 Possible Pixels in Volume	697169	14630318
R3 average width	36.48 km	39.98 km
R3 Precipitating pixels in Volume	347962	2065001
R3 Possible Pixels in Volume	1850577	22942410

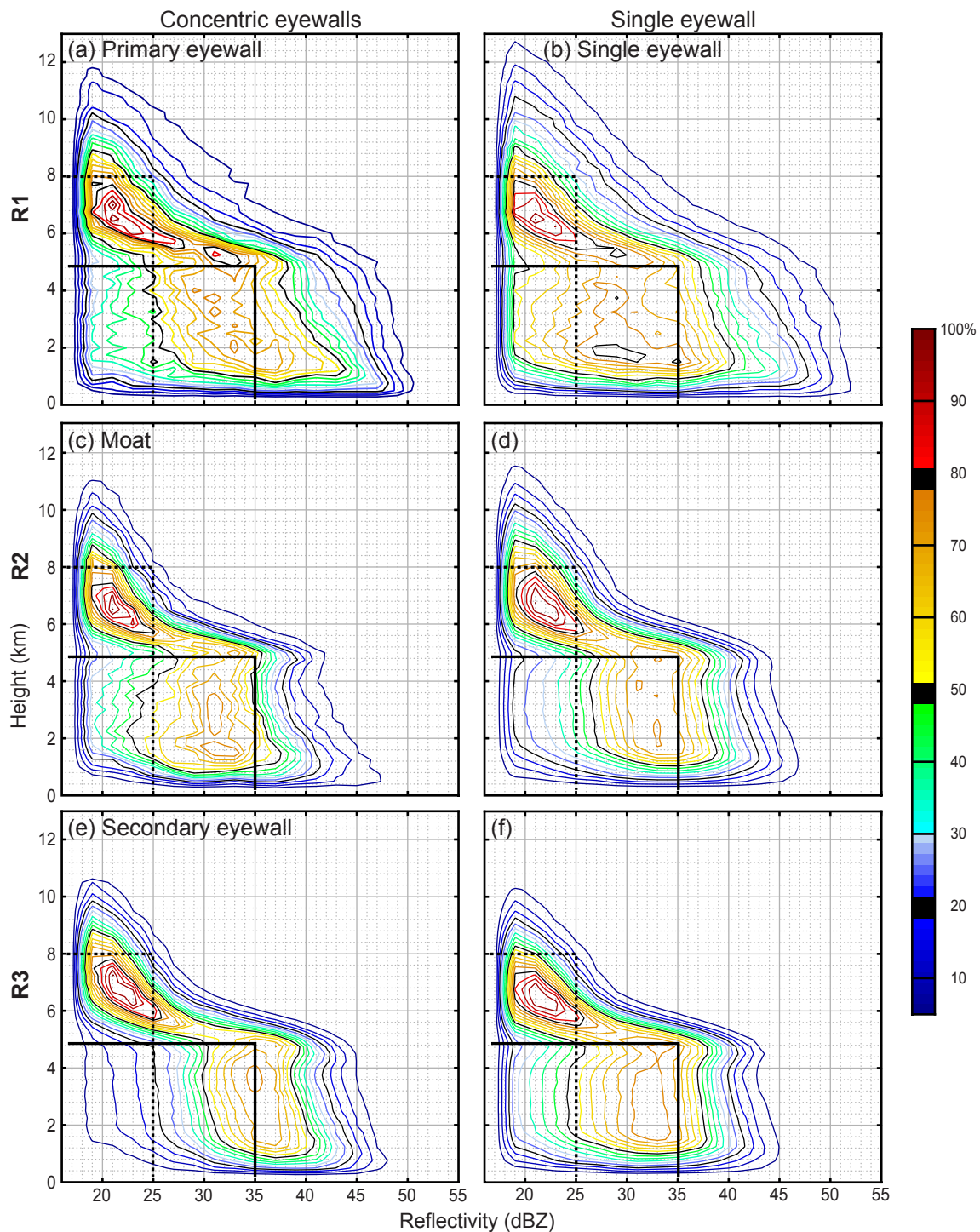


**Figure 1.** CFADs of TRMM PR reflectivity data for all of the 1998-2007 overpasses of storms that ultimately reached Category 4 or 5 intensity, for the total points of: a) region 1 (primary eyewall) of concentric eyewall cases; b) region 1 (single eyewall) of single eyewall cases; c) region 2 (moat) of concentric eyewall cases; d) region 2 of single eyewall cases; e) region 3 (secondary eyewall) of concentric eyewall cases; and f) region 3 of single eyewall cases. Contours represent the frequency of occurrence relative to the maximum absolute frequency in the data sample represented in the CFAD, contoured every 5%. Altitudes are geopotential height (km AMSL) relative to the ellipsoidal surface of the earth. The ordinate of the CFAD is altitude (in 250 m increments, or bins) and the abscissa is reflectivity in dBZ (in 1 dB bins). The 8 km and 25 dBZ levels are indicated by the black solid lines, and the 5 km and 35 dBZ levels are indicated by the black dotted lines for ease of reference. The 20%, 50%, and 80% contours are in black for reference.

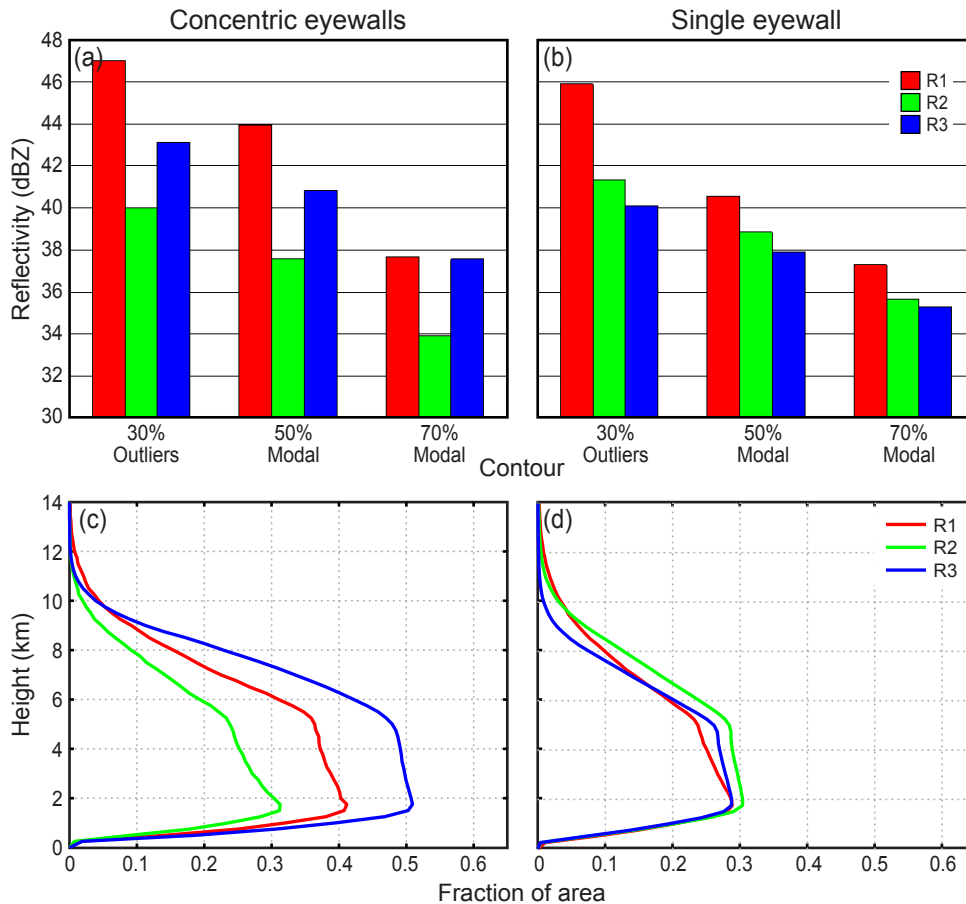


**Figure 2.** a) Maximum reflectivity reached below 4.5 km by the 30%, 50%, and 70% contours of the region 1 (primary eyewall, red bars), 2 (moat, green bars), and 3 (secondary eyewall, blue bars) concentric eyewall CFADs from Fig. 1a,c,e. b) Same as in a), but for the region 1 (single eyewall, red bars), 2 (green bars), and 3 (blue bars) single eyewall CFADs from Fig. 1b,d,f. c) Fractional areal coverage of accumulated reflectivity pixels as a function of height for region 1 (primary eyewall, red line), 2 (moat, green line), and 3 (secondary eyewall, blue line) of the concentric eyewall cases. d) Same as in c), but for region 1 (single eyewall, red line), 2 (green line), and 3 (blue line) of the single eyewall cases.

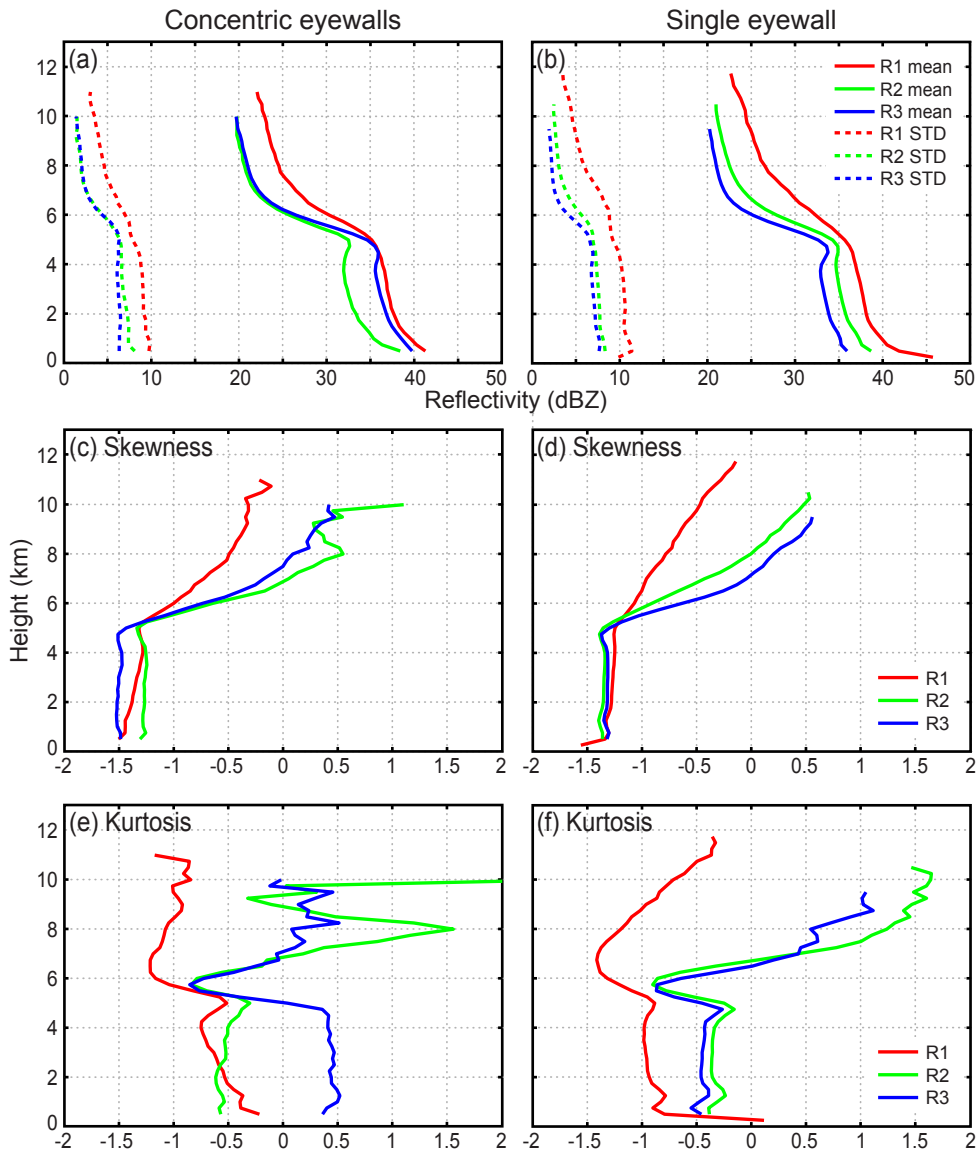


**Figure 3.** a) Mean reflectivity (solid lines) and standard deviation (dashed lines) as a function of height of region 1 (primary eyewall, red line), region 2 (moat, green line), and region 3 (secondary eyewall, blue lines) concentric eyewall CFADs. b) same as in a), but for the region 1 (single eyewall, red line), region 2 (green line), and region 3 (blue lines) single eyewall CFADs. c) Skewness as a function of height of region 1 (primary eyewall, red line), region 2 (moat, green line), and region 3 (secondary eyewall, blue lines) concentric eyewall CFADs. d) same as in c), but for the region 1 (single eyewall, red line), region 2 (green line), and region 3 (blue lines) single eyewall CFADs. e) Excess kurtosis as a function of height of region 1 (primary eyewall, red line), region 2 (moat, green line), and region 3 (secondary eyewall, blue lines) concentric eyewall CFADs. f) same as in e), but for the region 1 (single eyewall, red line), region 2 (green line), and region 3 (blue lines) single eyewall CFADs.

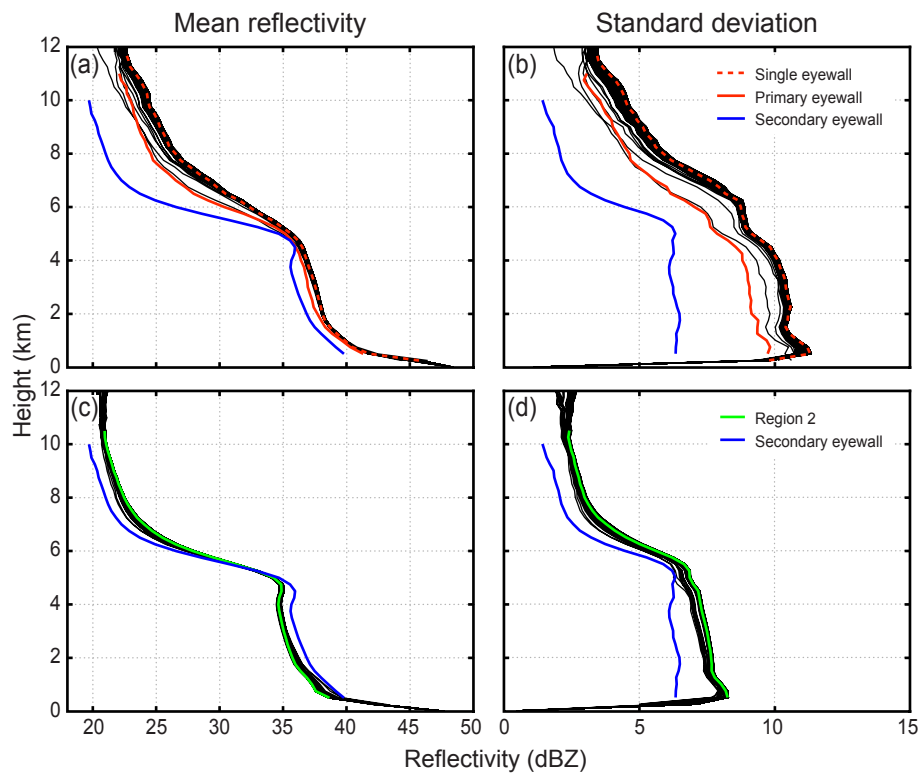


**Figure 4.** a) Mean reflectivity as a function of height of the total sample of the single eyewall (region 1, single eyewall cases), primary eyewall (region 1, concentric eyewall cases), and the secondary eyewall (region 3, concentric eyewall cases), with 1000 randomly chosen subsamples of the single eyewall region 1 data (black lines). b) Same as a), but for standard deviation. c) Mean reflectivity as a function of height of the total sample of region 2 of the single eyewall cases and the secondary eyewall (region 3, concentric eyewall cases), with 1000 randomly chosen subsamples of the single eyewall region 2 data (black lines). d) Same as in c), but for standard deviation.

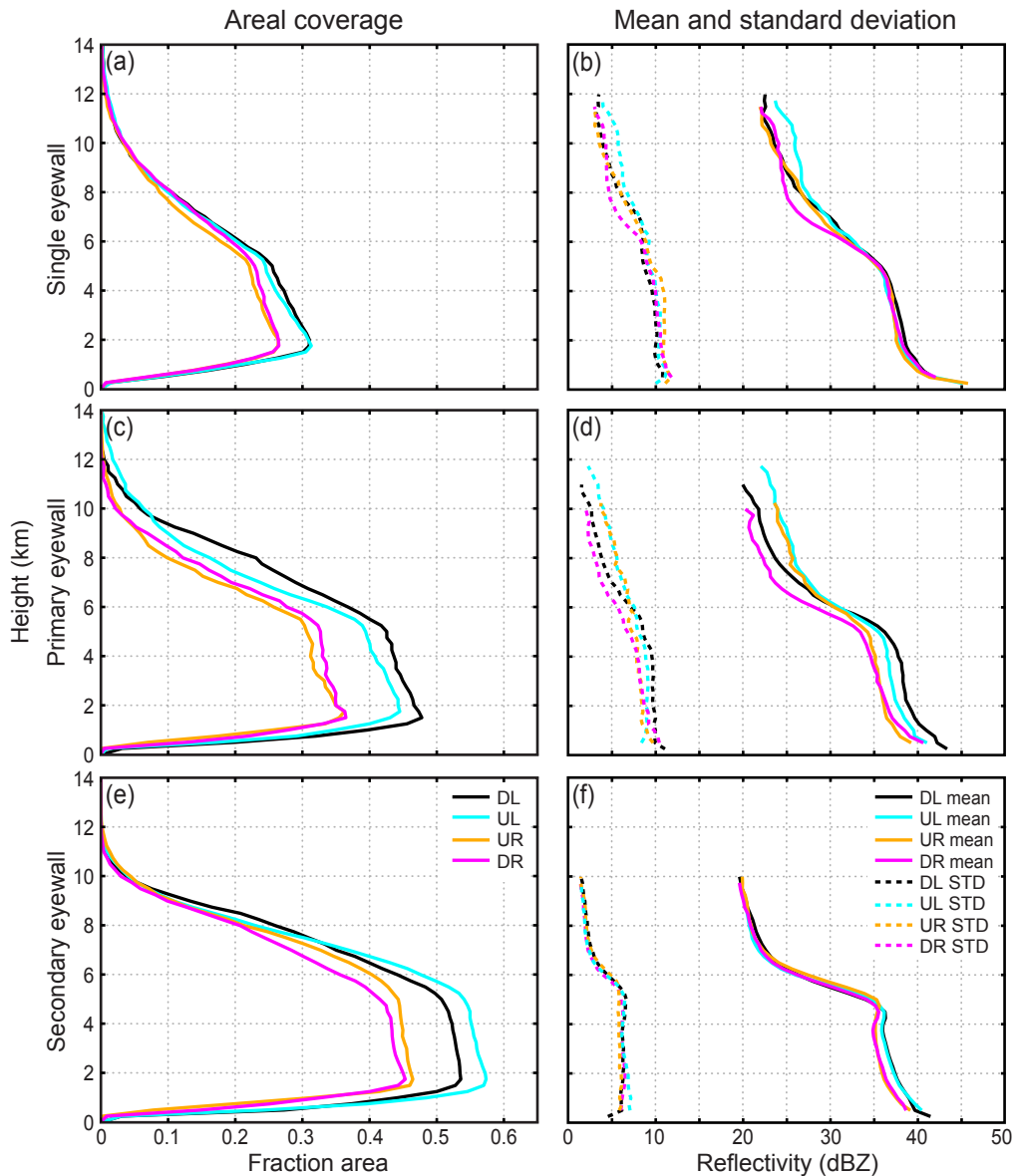


**Figure 5.** a) Percent of areal coverage of accumulated reflectivity pixels as a function of height for the downshear-left (black line), upshear-left (teal line), upshear-right (orange line), and downshear-right (magenta line) for the single eyewall cases (region 1, single eyewall cases). b) same as in a), but for the mean reflectivity (solid) and standard deviation (dash). c) same as in a), but for the primary eyewall (region 1, concentric eyewall cases). d) same as in c), but for the mean reflectivity (solid) and standard deviation (dash). e) Same as in a), but for the secondary eyewall (region 3, concentric eyewall cases). f) same as in e), but for the mean reflectivity (solid) and standard deviation (dash).

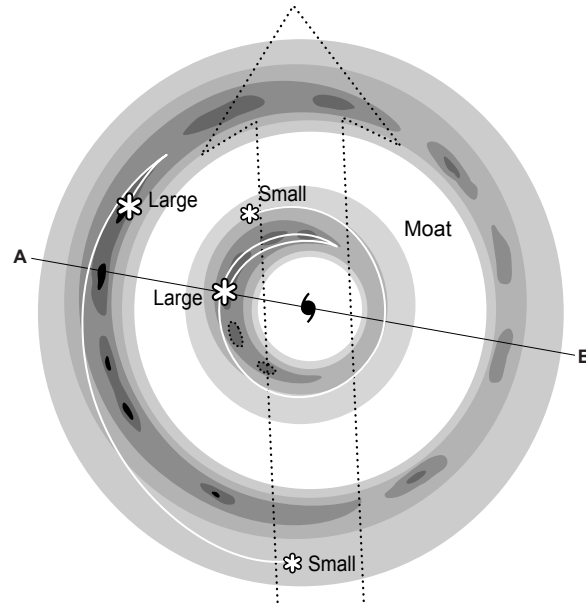


**Figure 6.** Idealized plan-view radar signature of the inner core of a tropical cyclone exhibiting concentric eyewalls overlaid with idealized particle trajectories. The shading represents radar reflectivity at intervals of 30, 35, 37.5, 40, and 45 dBZ. The small hurricane symbol represents the center of the cyclone. The first reflectivity ring represents the primary eyewall (region 1). The size of the convective cells indicates the level of maturity, with the dashed border indicating collapsing cells. The reflectivity-free region between the two eyewall features represents the moat (region 2). The outer reflectivity ring represents the secondary eyewall (region 3). The white curled lines represent the particle path, with the symbol representing where the particle would reach the surface. The dashed arrow represents the environmental shear vector. Line AB is a cross-section idealized in Fig. 7.

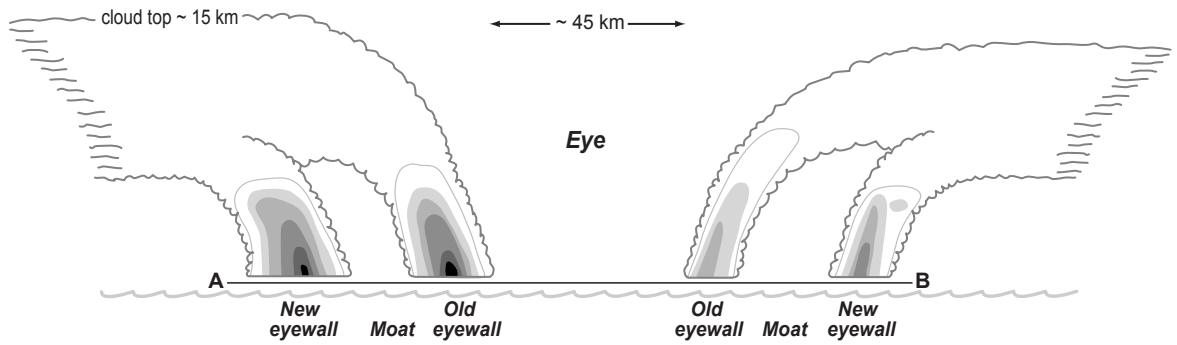


**Figure 7.** Idealized vertical cross-section along line AB of Fig. 6. Scalloped region represents the cloud boundary of the convective features. The shading represents radar reflectivity at intervals of 25, 30, 35, 37.5, 40, and 45 dBZ.